

Magnetic Focussing of ThO

Adam West

March 29, 2017

1 Introduction

Molecules exiting the beam source have a high divergence, meaning that only a very small fraction of them make it into the interaction region. To counter this we can focus the molecules. Development of an electrostatic lens is still ongoing, but here we consider using a magnetic lens as an alternative.

2 The Q State

The ground state and eEDM-sensitive states of ThO both have very small magnetic moments ($\sim 10^{-2} \mu_B$). Thus, to be able to magnetically focus the molecule beam, we must use a different state. The best option seems to be the Q state which is $^3\Delta_2$, meaning $S = 1$, $\Lambda = 2$ and $\Omega = 2$. $\Sigma = \Omega - \Lambda = 0$, so we can estimate the molecule frame g -factor as

$$G_{\parallel} = (g_L\Lambda + g_S\Sigma) = 2. \quad (1)$$

The rotational g -factor is then

$$g(J) = \frac{G_{\parallel}\Omega}{J(J+1)} = \frac{2 \times 2}{2(2+1)} = 2/3. \quad (2)$$

The maximum magnetic moment is in the $J = 2, M = 2$ stretched state, and is $4\mu_B/3$.

Using *J. Mol. Spec.* **113**, 93–104 (1985) we see that the transition wavelength from Q to C is around 1196 nm. Brendon did some work trying to get a laser diode to operate at that wavelength, but as far as I know, without success. The most effective way to populate the Q state is probably via STIRAP from X via C . Note that we would want to rotationally cool to $|X, J = 0\rangle$ beforehand.

3 Magnetic Field

In order to focus as many molecules as possible, we need to apply as large a magnetic field as possible, and we also need to produce a quadratic transverse potential. There are two main technologies available for producing large magnetic fields: permanent magnets or superconducting coils. The former is considerably technically easier, so we will consider that.

In a stretched state, the Zeeman shift is given by

$$E_Z = Mg(J)\mu_B|B|. \quad (3)$$

Here we ignore the possibility of any level crossings from neighbouring states. Thus, to produce a quadratic potential we need a quadratic field. This can be produced using a cylindrical Halbach array. The form of the magnetic field is given by e.g. *Nucl. Instr. Methods* **169**, 1–10 (1980) or *J. Mag. Mag. Mat.* **322**, 133–141 (2014). In the case of a continuous rotation of the magnetisation around the circumference of the cylinder, the magnetic field is given by

$$|B| = \frac{B_{\text{rem}}(k-1)}{k-2} \left[1 - \left(\frac{R_i}{R_o} \right)^{k-2} \right] \left(\frac{r}{R_i} \right)^{k-2} \quad (4)$$

where B_{rem} is the remanent magnetic flux density of the magnetic material, k indexes the multipole order, R_i is the inner radius of the cylinder, R_o is the outer radius and r is the radial position. Note that while $|B|$ is cylindrically

symmetric, \vec{B} is not. Note also that the above formula assumes a continuous rotation of the magnetisation around the cylinder which, in principle, can never be achieved.

A hexapole configuration ($k = 4$) produces a quadratic field shape given by

$$|B| = \frac{3B_{\text{rem}}}{2} \left(1 - \frac{R_i^2}{R_o^2}\right) \frac{r^2}{R_i^2}. \quad (5)$$

The maximum field is then achieved for $R_i/R_o = 0$ and $r = R_i$ (i.e. near the surface of the magnets and with a large outer radius) and is given by $B_{\text{max}} = 3B_{\text{rem}}/2$. The maximum value of B_{rem} currently available is 1.45 T from N52 grade Neodymium-Iron-Boron (NIB), giving $B_{\text{max}} = 2.18$ T.

For this field strength, the potential depth, in Kelvin, is given by

$$V = Mg(J)\mu_B B_{\text{max}}/k_B \quad (6)$$

$$= 2 \times 2/3 \times \mu_B \times 2.18 \text{ T}/k_B \approx 2 \text{ K}. \quad (7)$$

However, we will not be able to produce Halbach arrays with continuous magnetisation rotation, but rather with segments of uniform magnetisation. An analytic expression for the field from such an array is also provided in *Nucl. Instr. Methods* **169**, 1–10 (1980) and is shown below:

$$\tilde{B}(z) = B_{\text{rem}} \sum_{\nu=0}^{\infty} \left(\frac{z}{r_i}\right)^{n-1} \frac{n}{n-1} \left[1 - \left(\frac{r_i}{r_o}\right)^{n-1}\right] K_n \quad (8)$$

$$z = x + iy \Rightarrow B_x = \Re(\tilde{B}), B_y = \Im(\tilde{B})$$

$$n = N + \nu M$$

$$K_n = \cos^n(\epsilon\pi/M) \frac{\sin(n\epsilon\pi/M)}{n\pi/M}.$$

It is of course possible to compute the field using finite element analysis, e.g. in COMSOL, which I also did. The setup is illustrated in Fig. 1: A hexapole configuration cylindrical Halbach array was produced from 12 segments

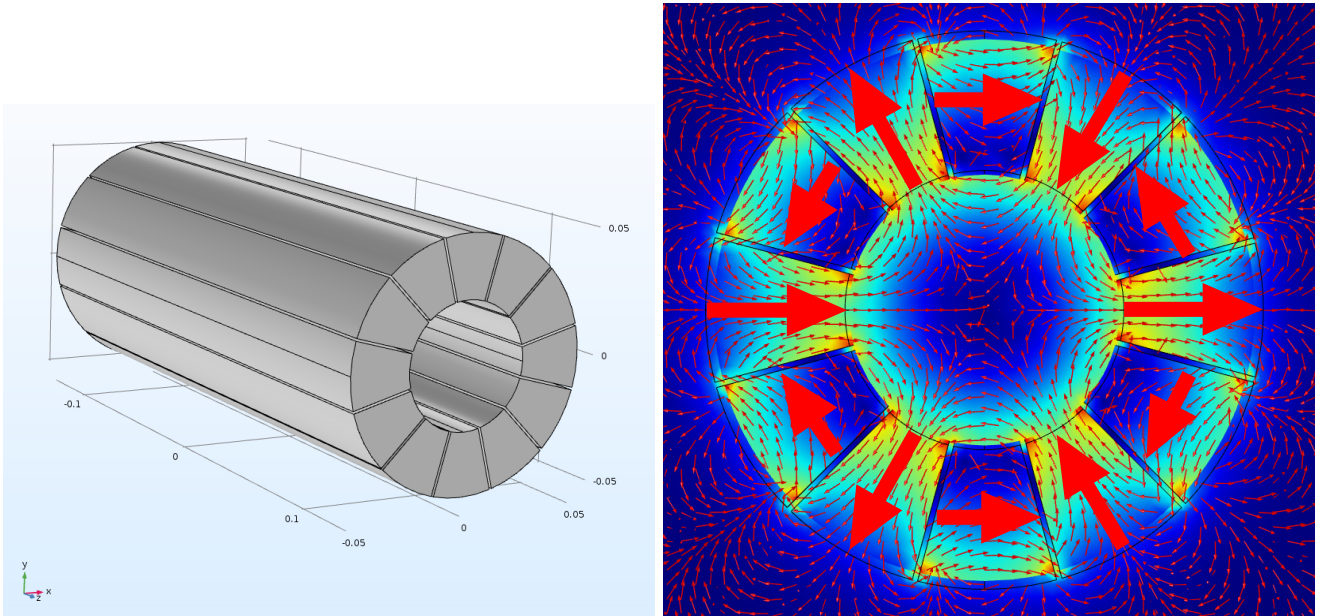


Figure 1: Left: Geometry of the magnetic material used in COMSOL — a hexapole cylindrical Halbach array. Right: Cross-section of the computed magnetic field. Large red arrows show the direction of the magnetisation of the segments. Small red arrows show the direction of the computed magnetic field. Colour shows the magnitude of the computed field.

of permanent magnetic material which is extended in the axial direction. There are small (1 mm) air gaps between the segments. The magnetisation directions of the segments are shown in the right-hand plot of Fig. 1, as well as the computed field — the size is indicated by the colour map, and the direction by the small red arrows.

A cross-section of the magnetic field from the axial centre of the array is shown in Fig. 2. We see there is a clear quadratic shape. Performing a polynomial fit of a line section of this field gives the functional form $1762r^2 + 2.6 \times 10^{-5}r + 1.5 \times 10^{-5}$ showing it is well represented by a pure quadratic.

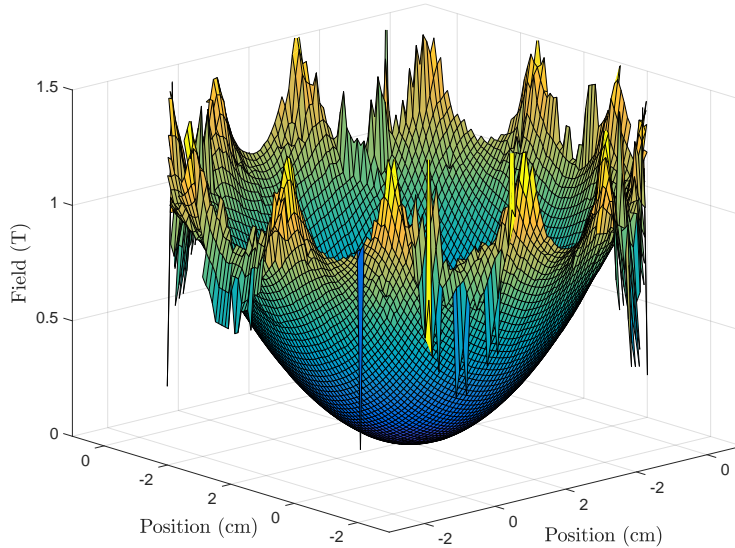


Figure 2: Cross-section of the magnetic field magnitude showing the quadratic shape.

We can make a comparison between the results from COMSOL and that from the analytic expressions to check for consistency. Fig. 3 shows a cross section of the field for both methods. These calculations assume: $r_i = 1$ in, $r_o = 2$ in, $B_{\text{rem}} = 1.4$ T, $k = 4$. We also assume the magnets are long in the axial direction. In the COMSOL model there is a gap between segments. Since this is defined in terms of a distance (1 mm), ϵ is not well defined. We use $\epsilon = 0.943$, which is the mean value between r_i and r_o for the specified gap. We see that there is good agreement between the two methods. Over the region shown, the mean difference in the size of the field is 17 mT. Fig. 4 shows slices through the field. The black solid traces are those provided by the analytic formula in Eq. 8. The black dashed lines are quadratic fits to these. We see that the quadratic fits are less accurate towards the edges of the region considered. The red solid lines are the equivalent slices taken from the field computed numerically by COMSOL. We see fairly good agreement, less faithful towards the edges. The dashed red lines are fits to these slices, showing similar behaviour to the analytic curves.

Altogether we see that the agreement between COMSOL and the analytic results is quite good. Let us now examine the maximum field that we can achieve. By repeating the calculations shown above we can plot the maximum field strength as a function of the outer radius of the array. We assume that the inner radius is 1 inch. The results are shown in Fig. 5. As expected, the ‘diagonal’ slice (red trace) which passes through the ‘peaks’ is significantly higher than the slice which passes through the ‘troughs’ (black trace). It is close to the overall maximum (blue trace), with the discrepancy being due to the discrete spatial grid. We find that we can fit the blue trace well with a double exponential curve of the form

$$B_{\text{max}}(r_o) = a - be^{-c(r_o-d)} - fe^{-g(r_o-h)}. \quad (9)$$

From this fit we find $a = 1.97$, which is an estimate of the maximum field strength achievable. If we ignore the gaps between segments, this maximum should be applicable for any inner radius too.

By comparison, we can compute the potential depth from an applied electric field for the ground state of ThO, which is shown below: For $J = 2, M = 0$, the state we are considering for electrostatic focussing, the maximum

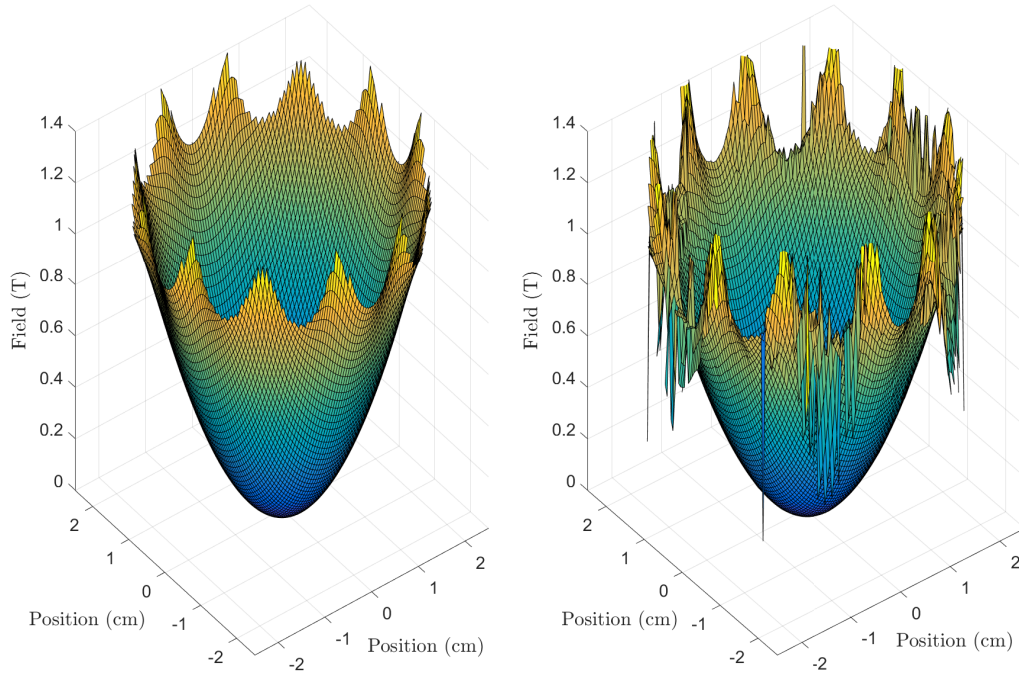


Figure 3: Left: Field computed via analytic expression. Right: Field computed via COMSOL.

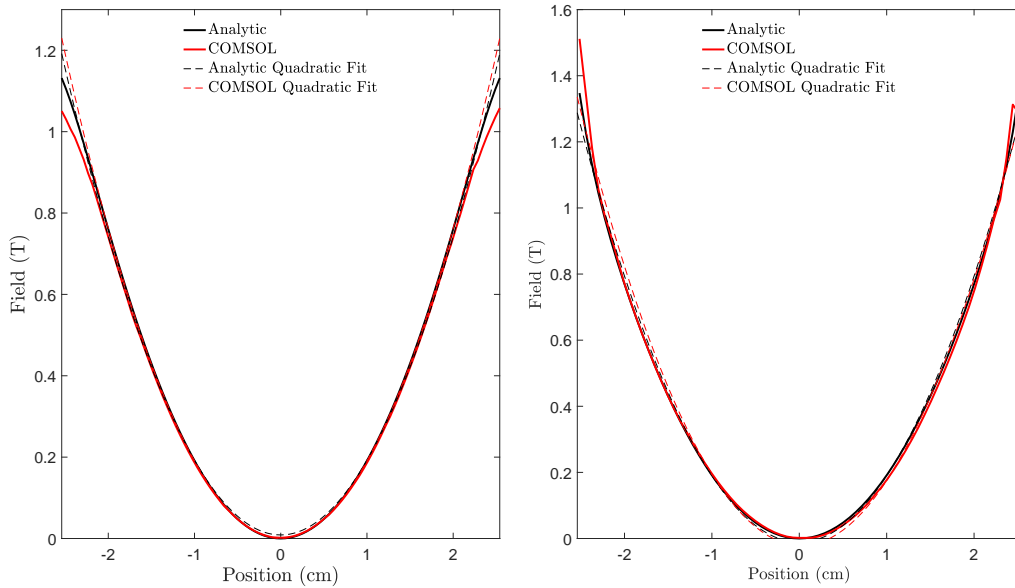


Figure 4: Left: Slices taken through the ‘troughs’ shown in Fig. 3, i.e. aligned with either of the position axes. Right: Slices taken at 45 degrees to the axes shown in Fig. 3.

potential depth is approximately 1 K. This suggests that there is the potential (!) for capturing more molecules

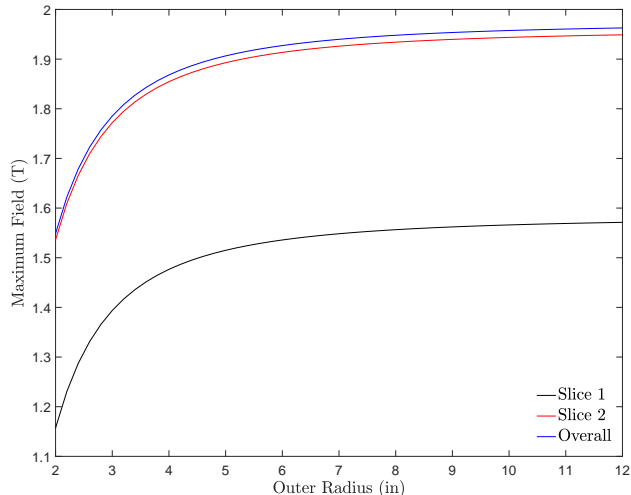


Figure 5: Maximum field strength as a function of the outer radius of the cylindrical Halbach array. The black traces are for a slice parallel to the position axes shown in Fig. 3. The red traces are for a slice at 45 degrees to these axes. The blue traces are the maximum field over the entire region.

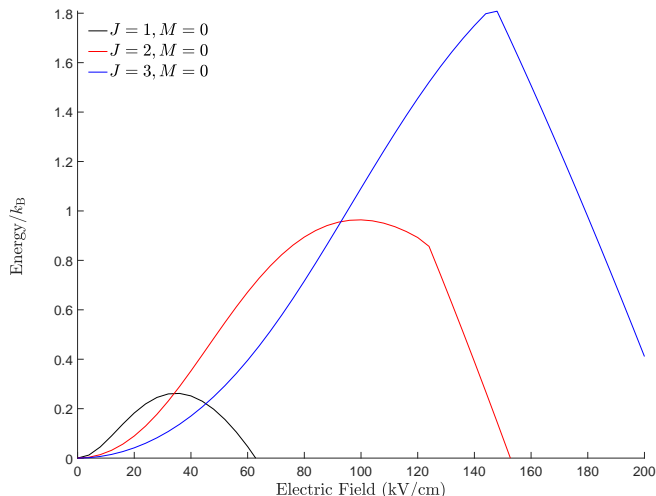


Figure 6: Computed Stark shifts for the X state of ThO. The rotational structure has been subtracted so that the potentials are all zero at zero E-field.

with a magnetic field.

We are also interested in knowing the fringing field from the Halbach array. It is likely that we will need to perform rotational cooling and STIRAP in close vicinity — if there is too large a magnetic field in that region it will jeopardise the efficacy of this process. From the computed field I found the maximum value of the magnetic field at every axial position, within a transverse distance equal to the magnets bore. The maximum field is then plotted for the region beyond the end of the array in Fig. 7. For these calculations I assume that the lens has an inner radius of 1 in. and an outer radius of 6 in. A smaller outer radius gives smaller fringing fields. We see that there is a significant fringing field present; at a distance of 10 cm from the Halbach array the maximum field is still more than 20 G.

In order to reduce the fringing fields we consider the addition of a yoke to the array. This consists of a soft

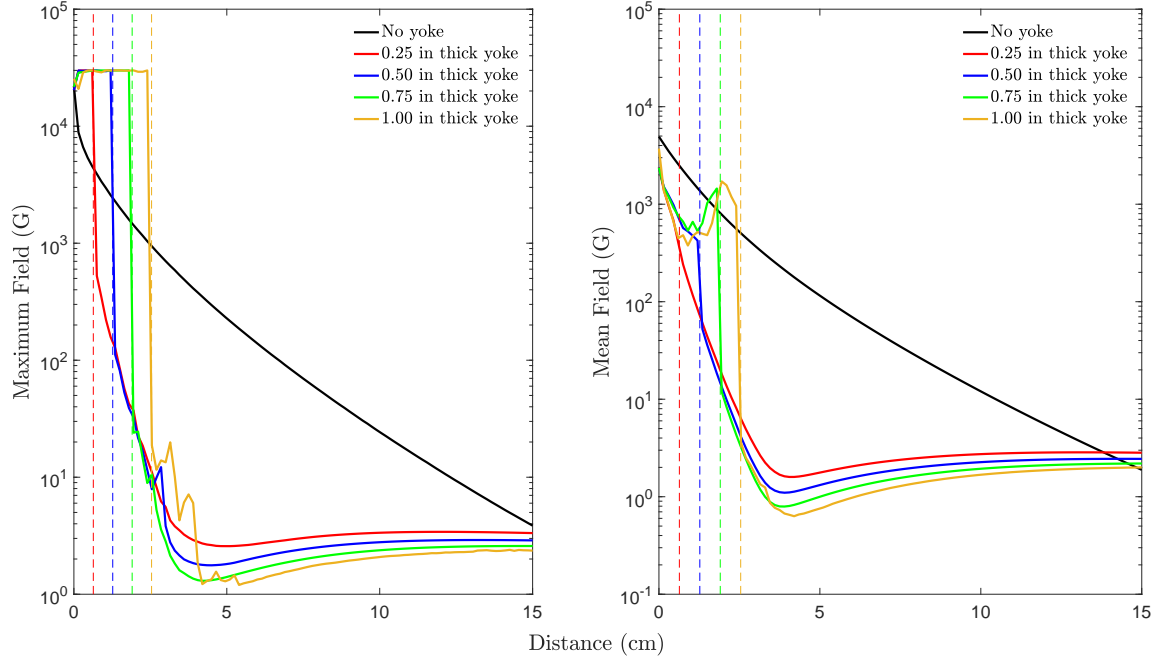


Figure 7: Left: Maximum magnetic field as a function of axial position from the end of the Halbach array. Note the log scale on the y-axis. Right: Mean field as a function of axial position. The dashed vertical lines show the extent of the yoke.

iron ‘horseshoe’ which provides a magnetically soft pathway that the field will follow in preference to extending out from the lens. Fig. 8 shows the yoke geometry as setup in COMSOL. The fringing fields were recomputed

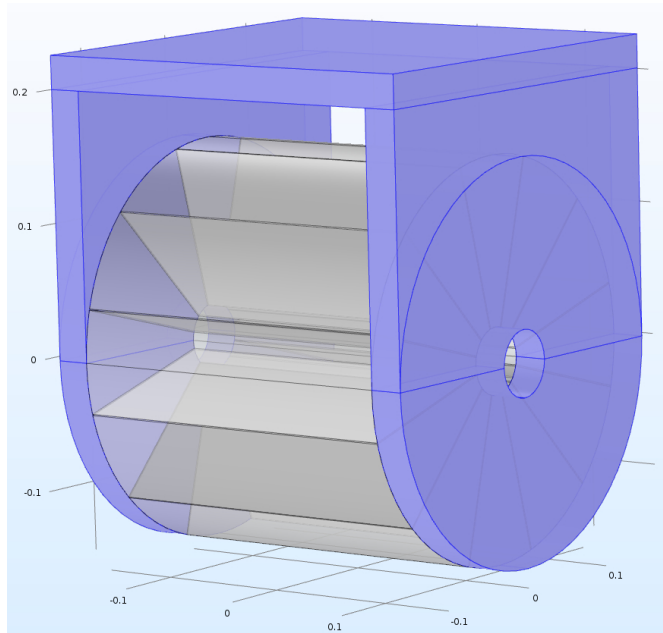


Figure 8: Yoke geometry within COMSOL.

with the addition of the yoke, for a number of different yoke thicknesses. The results of these calculations are also shown in Fig. 7. (Note that the maximum field is clamped at 3 T so as to ignore anomalously high fields due to numerical inaccuracies.) We immediately see that there is a large reduction of the fringing fields provided by the yoke. Far from the magnet the field is reduced to around 3 G. For all thicknesses of the yoke, the field is reduced below that value at less than 4 cm from the array. This kind of field size should be easily shimmed out by external coils if desired. However, it is not necessarily the size of the field that could be problematic. In fact it would be desirable to transfer molecules into the magnetically sensitive state in a region of non-zero field. This would permit adiabatic following of the magnetic field as the molecules enter (and leave) the lens. What is also important, is the uniformity of the field as this will affect the efficiency with which processes such as optical pumping and STIRAP can be performed. This is illustrated in Fig. 9. The left-hand plot shows the range of the field as a function of the

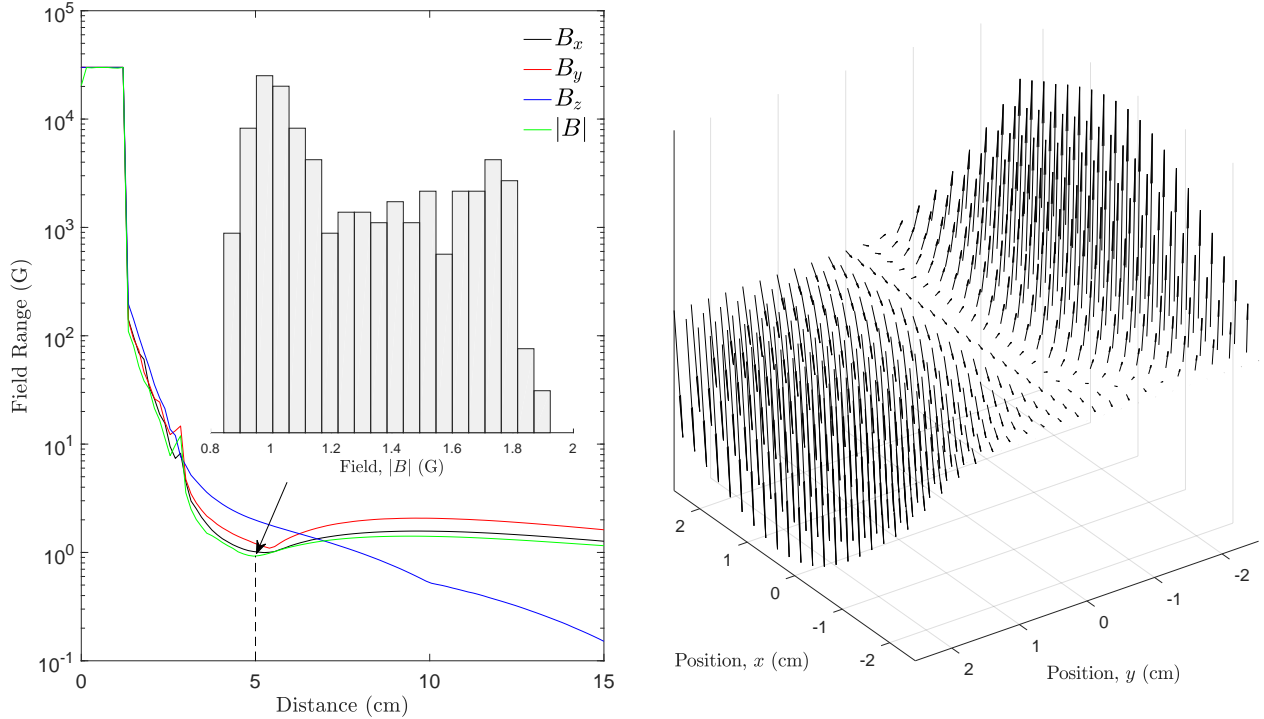


Figure 9: Left: Magnetic field range as a function of axial position, inset shows field distribution at 5 cm. Right: Cross-section of the field at a distance of 5 cm.

axial distance. It is computed as the maximum value minus the minimum value over a region equivalent to the lens bore ($r < 1$ in). We see that at the axial distance with the minimum fringing field the range of the field is around 1 G, which corresponds to a frequency range of 1 MHz — this is small compared to the Doppler width so should not jeopardise any state preparation schemes that are performed in this region. The z component of the field has a significantly larger variation than the other cartesian components — this is the axial direction. In the inset is a histogram of the magnitude of the magnetic field at a distance of 5 cm. We see a fairly uniform distribution. The right-hand plot shows a map of the field at an axial distance of 5 cm. The magnitude and direction of the field are represented by the arrows. It is interesting to note that there is significantly more variation in the field along the y direction than the x direction. This is perhaps intuitive when considering the magnetisation pattern of the Halbach array. Referring to the right-hand side of Fig. 1, the vertical (horizontal) direction corresponds to the x (y) axis. One can see that the magnetisations of the segments on the y axis are aligned and have exposed poles. One can then imagine magnetic field lines wrapping around in the yz plane producing a larger field variation along y than x .

4 Trajectory Simulation

4.1 Calculating Molecule Flux Gain

4.1.1 Lens Length and Inner Radius

I have performed numerical simulations of the trajectories for molecules being focussed by a hexapole Halbach array. Fig. 10 shows the setup assumed. Molecules exit the cell aperture, but the simulation begins at the zone

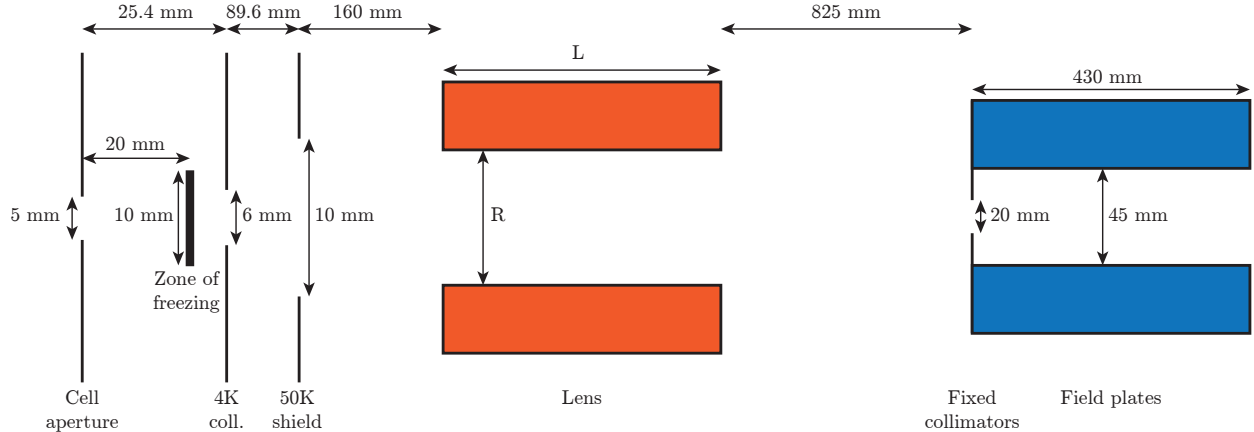


Figure 10: Schematic of the setup used in trajectory simulations.

of freezing, which we assume to be 2 cm away. The transverse position distribution is uniform and the transverse velocity distribution is Gaussian. The molecules then pass through the 4 K collimator. The 50 K and beam box apertures are ignored since they do not collimate any further molecules. The molecules pass into the magnetic lens where they are focussed. The field within the lens is computed analytically assuming a simple quadratic form, maximally 2.1 T at the surface of the magnets. The molecules then pass through the interaction region collimator and between the field plates. Molecules are considered successful if they do not hit any collimators, or the lens, or the field plates, and reach the end of the interaction region. The fraction of molecules that are successful is counted, and then compared to the fraction without the lens in place (accounting for the change in beamline length) to compute the gain.

Fig. 11 shows the dependence of the molecule number gain on the length and inner radius of the magnetic lens. We see that a maximum gain of around 15 can be achieved. This can be achieved for a range of different lens lengths — the inner radius must be increased as the length is increased. The length is limited, however, as at some point the capture range becomes limited simply by geometry, rather than by the potential depth. We also see that there is a secondary band where there is significant gain, for high lens length — this is where the molecules oscillate twice inside the lens (the length is tripled for such trajectories).

We repeat this calculation for a couple of different maximum field values — in reality is unlikely that we shall be able to achieve 2.1 T. Fig. 12 shows the gain achieved when we instead assume maximum fields of 1.9 T and 1.6 T. We see that reducing the maximum field from 2.1 T to 1.9 T has very little change on the gain achieved. Reducing to 1.6 T gives a small decrease in the achievable gain. Note, however, that this may be because the lens length required increases as the field decreases.

We can perform a slightly more faithful calculation if we use the field calculated for a segmented array, as given by Eq. 8. In this case the maximum field is not specified, but calculated assuming an outer radius of 6 in. An important difference is that the field now has azimuthal dependence. During the trajectory calculation we take the field calculated per Eq. 8 (which assumes infinite axial extent) and apply it at all points within the lens length, interpolating at the molecule positions. Fringing fields are ignored. Performing this calculation yields Fig. 13. We see a very similar result to the case using a simple quadratic field with 1.6 T maximum size. Now let's look a little more closely at these results. Fig. 14 shows the dependence on length of the gain with a specified inner radius, again assuming a 6 in outer radius. We see that with an inner radius of 0.5 in. a maximum gain of around 9 is

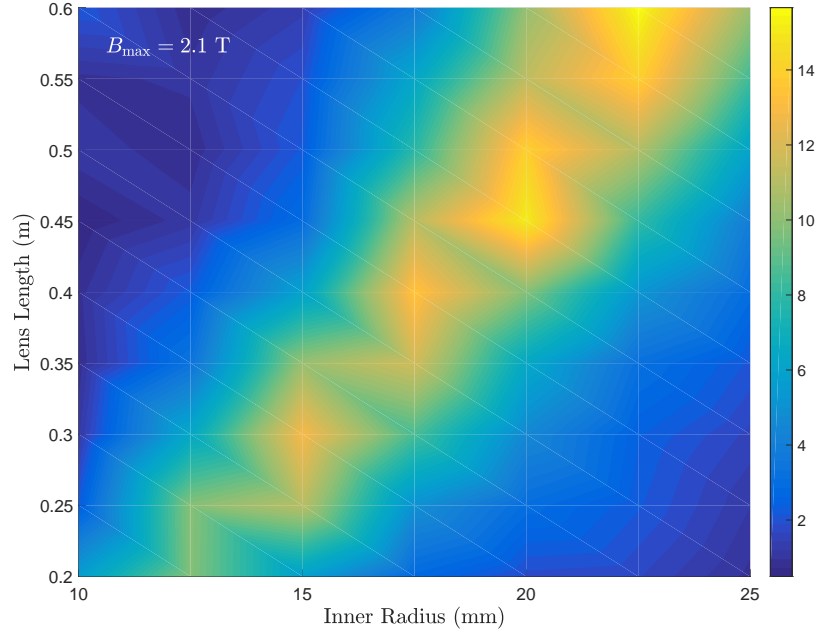


Figure 11: Molecule gain as a function of the length and inner radius of the magnetic lens. We assume a simple quadratic form of the field with a maximum value of 2.1 T.

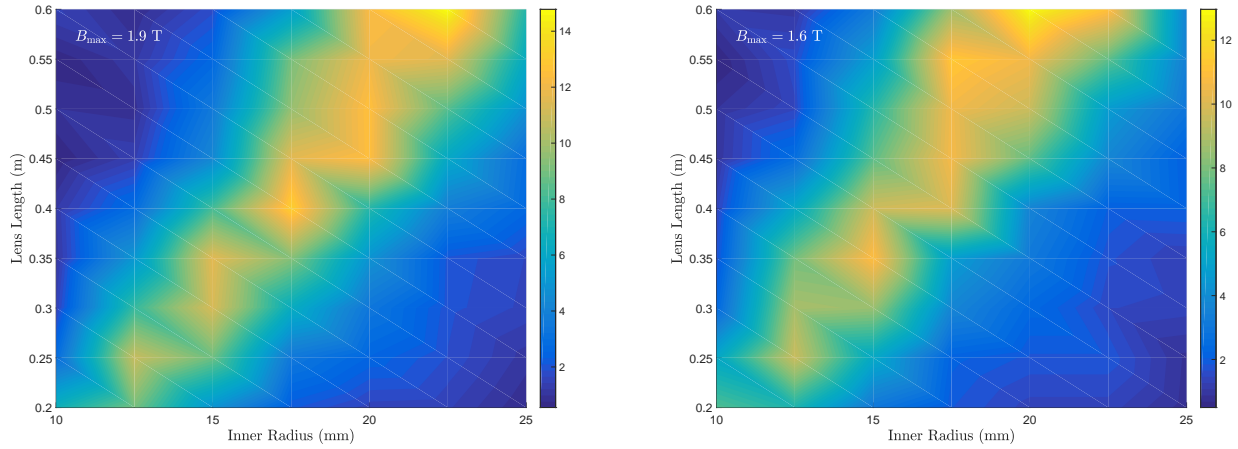


Figure 12: Molecule gain as a function of the length and inner radius of the magnetic lens. We assume a simple quadratic form of the field with a maximum value of 1.9 T (left) or 1.6 T (right).

achieved for a lens length of approximately 25 cm. If the inner radius is enlarged to 2 cm, the achievable gain goes up to around 11, but the required length is significantly higher, at around 55 cm.

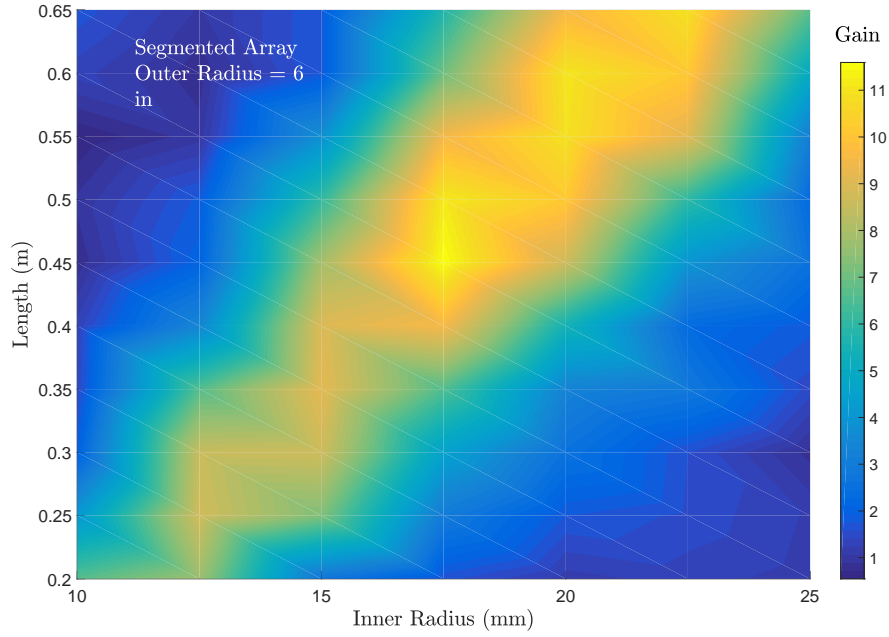


Figure 13: Molecule gain as a function of the length and inner radius of the magnetic lens. We use an analytic form of the field for a segmented array, assuming a 6 in outer radius.

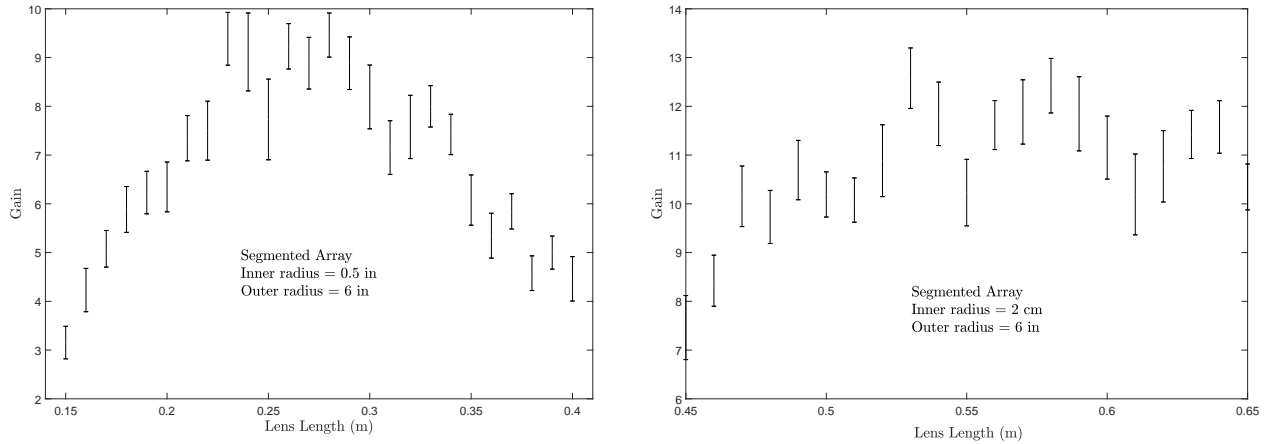


Figure 14: Molecule gain as a function of lens length for the case of a segmented array, with field calculated using Eq. 8, assuming a 6 in outer radius.

4.1.2 4 K Collimator

Until now we have made some assumptions about the molecule beam that may be inaccurate, or about the beam box which could be changed. In particular we have assumed that the zone of freezing of the molecules is 2 cm downstream of the cell aperture and the effective source size is 1 cm in diameter. We don't know whether this is accurate. In fact, recent data taken by Elizabeth in the thermochemical beam source suggest that collisions could be frozen out by 1 cm downstream of the cell. The 6 mm diameter of the 4 K collimator was chosen for a number of reasons: it was how the beambox was characterised and we didn't want to mess with a good thing; the aperture was designed in Gen. 1 where its aperture was more comparable to the field plate collimator size; it kept the gas load reasonably low. However, it may be that we can change its size and get more flux. I examine this possibility here. I ran trajectory simulations changing the size of the 4 K collimator. The results are shown in the left-hand plot of Fig. 15. I then repeated the analysis assuming that the zone of freezing is 1 cm from the cell, rather than 2 cm, and the effective source diameter is 0.75 cm (half way between the cell aperture size and the previously assumed 1 cm). The results for these simulations are shown in the right-hand plot of Fig. 15.

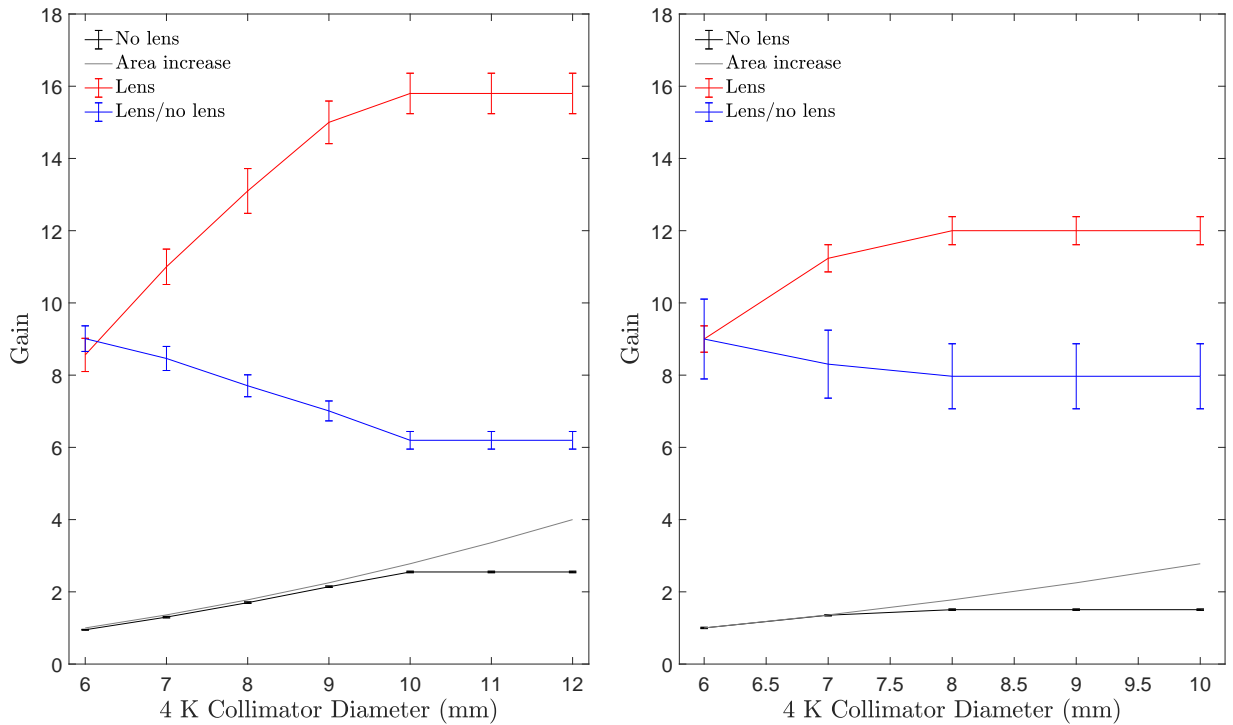


Figure 15: Predicted gain vs the diameter of the 4 K collimator in the beam box. Left (Right): assuming a zone of freezing diameter of 1 cm (0.75 cm) and a distance of 2 cm (1 cm) from the cell aperture. Black traces show the expected gain without including a magnetic lens. Grey lines indicate the increase in area of the 4 K collimator. Red traces show the expected gain with a magnetic lens in place (inner radius 0.5 in, length 25 cm). The blue trace is the gain with the lens divided by the gain without, i.e. showing the gain achieved just from the inclusion of the lens.

We see that the effect of opening up the 4 K collimator alone scales approximately with the area increase (black and grey traces). This is intuitive since the zone of freezing is close to this collimator and molecules with an initial transverse position outside the 4 K collimator are almost certainly lost. If we consider the inclusion of a magnetic lens we see that there is also a significant increase in the gain (red). Taking the ratio of the two gains to extract the effect of the lens alone we see that with the larger collimator size the obtained gain is slightly less. One can explain this intuitively by considering that the 'new' molecules accessed by opening up the collimator are more likely to be useful if there is no lens in; molecules with high initial transverse position are slightly less likely to make it to the

detection region if there is lens in.

When we repeat this analysis with a smaller and further upstream zone of freezing we see that the general behaviour is the same but the size of the effect is less. With a smaller zone of freezing the 4 K collimator is cutting out fewer molecules, so less is gained by opening it up. In this case there is very little change in the utility of the lens as the collimator is made larger.

4.2 Protecting the Field Plates

It seems then that there is strong evidence to suggest we can achieve around an order of magnitude greater flux using magnetic focussing with field strengths realistically achievable from permanent magnet arrays. However, we have yet to comment on another important aspect of the focussing — we must ensure that none of the focussed molecules impinge on the field plates. Fortunately this analysis is straightforward: in all of the simulations presented here, zero molecules hit the field plates.

4.3 Molecule Beam Properties

It will be of vital importance to know the spatial and velocity distributions of the molecule beam in order to assess how effectively we can perform state preparation and transfer (see Sec. 5). To characterise these properties I simply ran trajectory simulations for a particular set of lens parameters, collated the successful trajectories and used these to plot the relevant distributions. The results are shown in the following figures. I assume a 0.5 in inner radius, 6 in outer radius, 25 cm lens length and use the analytic form of the field for a segmented array.

First, Fig. 16 shows the spatial distributions of the molecules, plotted at longitudinal positions of 5 cm before and 5 cm after the lens in both of the transverse directions: We see that the spatial distributions are quite flat, which is perhaps expected as the initial distribution, at the zone of freezing is assumed to be uniform — there is some fall off at the edges as these molecules have varying probability to make it through the system, depending on their transverse velocity. We also note that the distributions are symmetric in the two transverse axes, as expected. Perhaps most interesting is the fact that the transverse size of the beam is greater after the lens.

We can perform a similar analysis for the transverse velocity distributions, shown in Fig. 17. Again, the shapes of the distributions are fairly intuitive. Before the lens we are selecting a fairly small central region from a broad Gaussian distribution, giving a reasonably flat shape, and there is again symmetry between the axes. It is interesting to note that there is a significant decrease in the width of the velocity distribution after the lens, and a more Gaussian shape is observed. It seems that we are trading decreased velocity width for increased spatial width. This can be seen more clearly in Fig. 18.

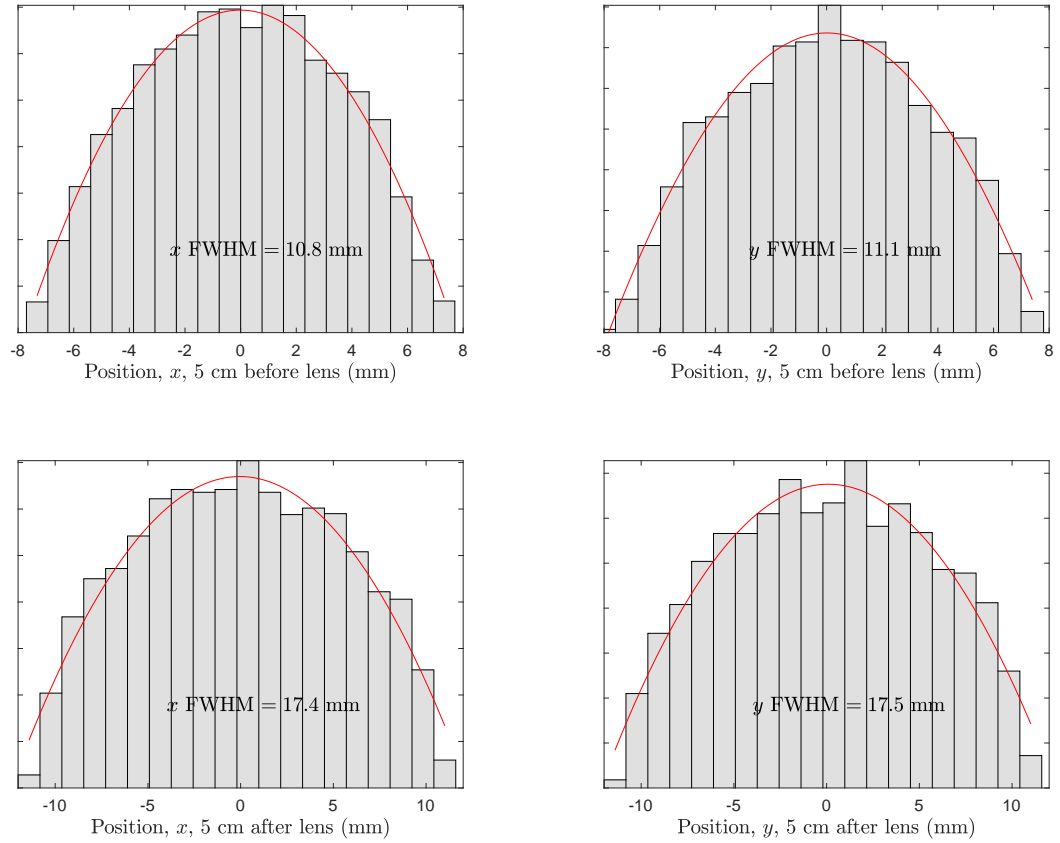


Figure 16: Spatial distributions of the molecule beam in the transverse directions at axial positions 5 cm before and 5 cm after the lens. Uses analytic form for segmented array with inner radius of 0.5 in and outer radius of 6 in.

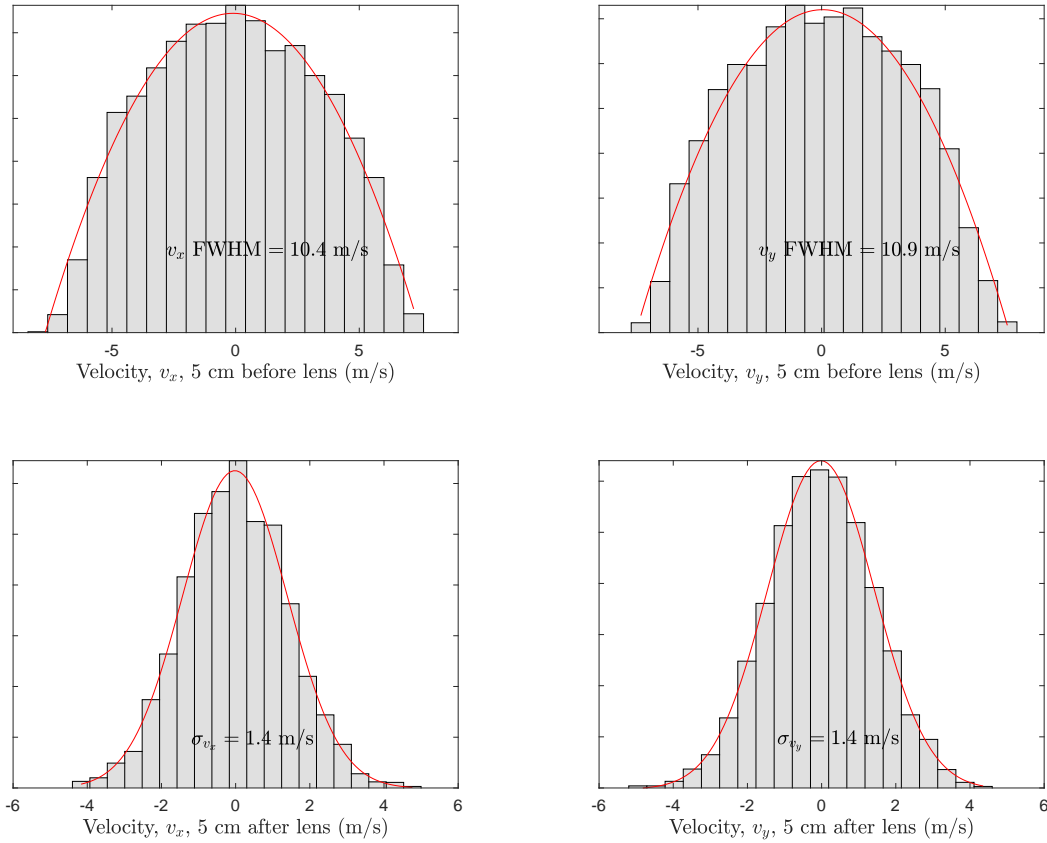


Figure 17: Velocity distributions of the molecule beam in the transverse directions at axial positions 5 cm before and 5 cm after the lens. Uses analytic form for segmented array with inner radius of 0.5 in and outer radius of 6 in.

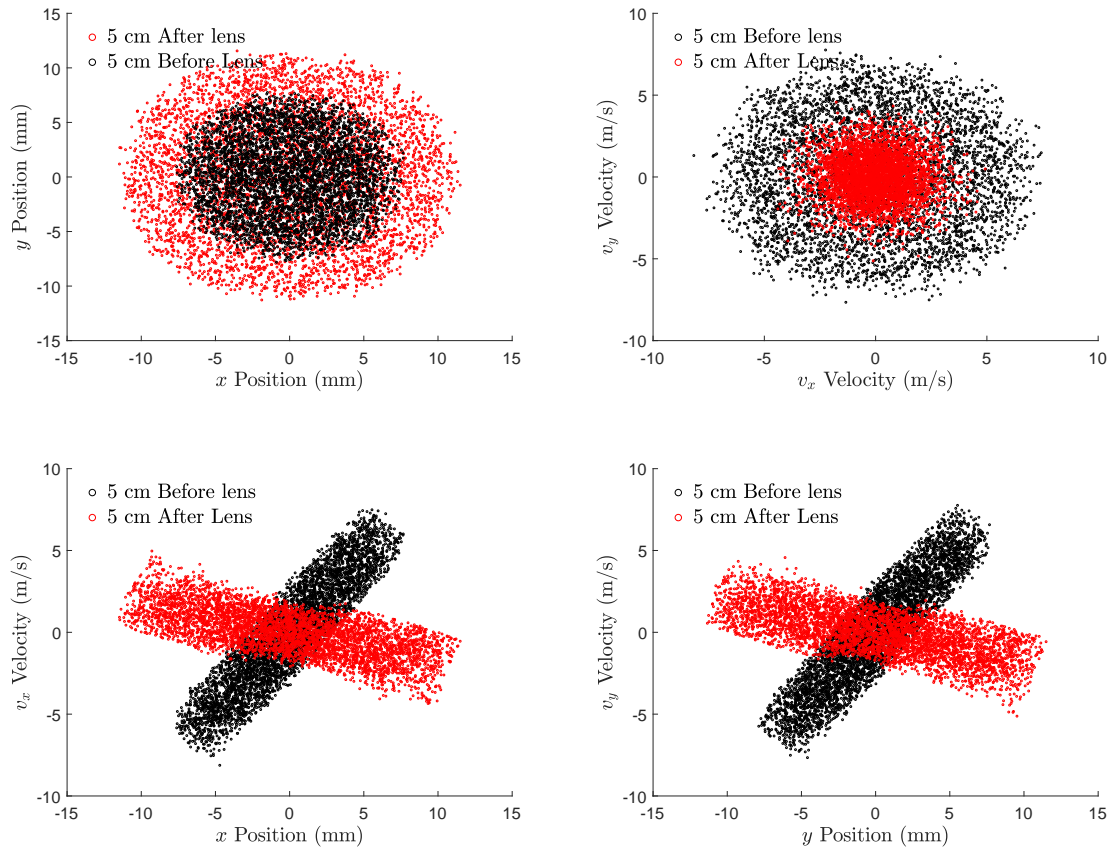


Figure 18: Phase space maps of the molecule beam in the transverse directions at axial positions 5 cm before and 5 cm after the lens. Uses analytic form for segmented array with inner radius of 0.5 in and outer radius of 6 in.

State	Ω	Term Symbols	Pump (nm)	Pump μ (D)	Stokes (nm)	Stokes μ (D)	τ (ns)	P_1 (mW)	P_2 (mW)	P_3 (μ W)	P_4 (μ W)
X	0	$^1\Sigma^+$	-	-	-	-	∞	-	-	-	-
Q	2	$^3\Delta_2$	-	-	-	-	-	-	-	-	-
B	1	76.5% $^3\Pi$, 17.8% $^1\Pi...$	899		2000						
C	1	76.6% $^1\Pi$, 19.5% $^3\Pi...$	690	1.5	1196	≈ 1	468	3.9	0.2	103	36
D	1	74.5% $^3\Sigma^+$, 14.6% $^3\Phi...$	627		1018						
I	1		512	1.84	745	0.59	115	4.7	1.9	90	105
K	1		442		606						
L	1		402	2.94	536	1.42	17	3.0	33.5	31	18
M	1		460		641						
N	1		361		463						
U	1		397	1.08	526	1.28	57	22.7	22.1	119	31

Table 1: Various properties for all known $\Omega = 1$ states in ThO. Pump = transition wavelength between X and the state, Pump μ = transition dipole moment for this transition, Stokes = transition wavelength between the state and Q , Stokes μ = transition dipole moment for this transition. Consult main text for descriptions of P_1 , P_2 , P_3 and P_4 . All values are approximate — consult references for further details: [1, 2, 3, 4].

We see in the bottom plots that the phase space is rotated and stretched along the spatial dimension. The rotation changes the sign of the velocity/position gradient, corresponding to the reversal of the trajectories during focussing. The stretching in the spatial direction reflects the previously described ‘trade’ of velocity width for spatial width, seen most clearly in the top plots of Fig. 18.

These data seem to reinforce the idea that the optimal configuration can be thought of as weakly focussing the beam — taking a strongly diverging section of the molecule beam and making it weakly converging.

5 Molecule State Preparation

In order to take advantage of any magnetic lens, we must be able to efficiently transfer molecule population to and from the magnetically-sensitive state. The general scheme to do this would most likely consist of performing rotational cooling as normal, i.e. concentrating population in the $|X, J = 0, M = 0\rangle$ state, and then performing STIRAP transfer into the state of interest, i.e. $|Q, J = 2, M = 2\rangle$. There are a number of possible options for the intermediate state, which should have $\Omega = 1$ such that we can transfer through a $|J = 1, M = 1\rangle$ state. All known $\Omega = 1$ states are shown in Table 1 together with some of the relevant properties. We don’t have an accurate measurement of the transition dipole moment, μ , for $Q \rightarrow C$ but we can estimate it. Ref. [2] gives a handy formula in Eq. 3:

$$\mu = \sqrt{\frac{b}{3.137 \times 10^{-7} \nu^3 \tau}} \quad (10)$$

where b is the branching ratio and ν is the transition energy in wavenumbers. Assuming $b = 0.1$ we get $\mu \approx 1$ D.

As an aside, note that the relevant transition dipole moment is found by taking into account branching between rotational levels and the particular M sublevel being driven to/from. The relevant equations for this can be found e.g. in Nick’s thesis, Section 2.4 onwards. Following this, we can use

To quantitatively assess the suitability of the transitions, let us first consider the case of optical pumping. It is important that: a) our laser beams address the entire molecule beam, b) our laser beams interrogate the molecules sufficiently strongly/for sufficient time that optical pumping is effective. Let’s consider a) first.

From Dave’s book, Eq. 3.176 and following, we see that in order to address the entire Doppler width we require

$$\sqrt{1 + \kappa} \gg \Gamma_D \tau, \quad (11)$$

where κ is the saturation parameter, Γ_D is the Doppler width and $\tau = 1/\gamma_0$ is the natural lifetime. I note that

there is a factor of $\sqrt{2}$ between Γ_D and $\sigma_{v_{x,y}}$. I also rewrite κ using Eq. 3.159, giving

$$\sqrt{1 + \frac{\tau^2 d^2 \mathcal{E}_0^2}{\hbar^2}} \gg \tau \sqrt{2} \sigma_{v_{x,y}} \quad (12)$$

$$\sqrt{1 + \Omega^2 \tau^2} \gg \tau \sqrt{2} \sigma_{v_{x,y}}. \quad (13)$$

where Ω is the Rabi frequency. If we assume $\Omega^2 \tau^2 \gg 1$ we have

$$\Omega \gg \sqrt{2} \sigma_{v_{x,y}}. \quad (14)$$

We see then that we can expect to address the entire Doppler width if the Rabi frequency is the largest frequency in our system, greater than both the decay rate and the Doppler width. A useful metric then, is the required power such that $\Omega = \max(1/\tau, \sqrt{2}\sigma_{v_x})$. For this we must make some assumptions about the laser beam size. The long dimension should be guided by the spatial distributions shown in Fig. 18 — let's set the beam waist in the long dimension to be 2 cm. The width is then limited by what is reasonable, let's choose a waist of 1 mm here. The power in a Gaussian beam is given by

$$P = \frac{1}{2} \pi w_x w_y I_{\text{peak}} \quad (15)$$

where w_x, y are the beam waists and I_{peak} is the peak intensity, which is given by

$$I = \frac{1}{2} c \epsilon_0 |\mathcal{E}_{\text{peak}}|^2 \quad (16)$$

in vacuum, where c is the speed of light, ϵ_0 is the permittivity of free space and $\mathcal{E}_{\text{peak}}$ is the peak amplitude of the electric field. Using these equations, and the fact that $\Omega = d\mathcal{E}/\hbar$ for a transition dipole moment, d , we get

$$P = \frac{1}{4} \pi w_x w_y c \epsilon_0 |\mathcal{E}_{\text{peak}}|^2 \quad (17)$$

$$= \frac{1}{4} \pi w_x w_y c \epsilon_0 \frac{\hbar^2 \Omega_{\text{peak}}^2}{d^2}. \quad (18)$$

If we assume that the average intensity in the laser beam is half that at the peak then the average rabi frequency is a factor of $\sqrt{2}$ smaller and we then have

$$P = \frac{1}{2} \pi w_x w_y c \epsilon_0 \frac{\hbar^2 \Omega_{\text{avg.}}^2}{d^2}. \quad (19)$$

We can then calculate the power required to ensure that the average Rabi frequency is equal to $\sqrt{2}\sigma_{v_{x,y}}$ or $1/\tau$

$$P_1 = \pi w_x w_y c \epsilon_0 \frac{\hbar^2 \sigma_{v_{x,y}}^2}{d^2} \quad (20)$$

$$P_2 = \pi w_x w_y c \epsilon_0 \frac{\hbar^2}{2\tau^2 d^2}. \quad (21)$$

I have made a spreadsheet for computing these quantities which can be found here. I include the calculated values of P_1 and P_2 in 1. We find that for rotational cooling on $X \rightarrow C$ we need around 4 mW (0.3 mW) of power for an average Rabi frequency equal to the Doppler width before the lens (natural linewidth). Note that this power depends quadratically on Rabi frequency, so if we want the Rabi frequency to exceed these two frequencies by a factor of 10 we will need 400 mW.

To determine how much power is needed for efficient rotational cooling is a more difficult question which is better suited to simulation of rate equations — something which Zack has previously done.

Now let's consider the requirements for STIRAP. Firstly, the adiabaticity criterion is given by

$$\Omega_{\text{eff}} \delta t \gg 1 \quad (22)$$

where $\Omega_{\text{eff}} \equiv \sqrt{\Omega_{\text{Pump}}^2 + \Omega_{\text{Stokes}}^2}$ is the effective Rabi frequency and δt is the transit time through the STIRAP beams. We can then make a reasonable estimate of where $\Omega_{\text{eff}}\delta t = 1$. Rearranging Eq. 19 we have

$$\Omega_{\text{avg}} = \sqrt{\frac{2d^2P}{\pi w_x w_y c \epsilon_0 \hbar^2}} \quad (23)$$

$$\Rightarrow \Omega_{\text{eff}} = \sqrt{\frac{2d_{\text{Pump}}^2 P_{\text{Pump}}}{\pi w_x w_y c \epsilon_0 \hbar^2} + \frac{2d_{\text{Stokes}}^2 P_{\text{Stokes}}}{\pi w_x w_y c \epsilon_0 \hbar^2}}. \quad (24)$$

If we assume that $P_{\text{Pump}} = P_{\text{Stokes}} = P$ then

$$\Omega_{\text{eff}} = \sqrt{\frac{2P(d_{\text{Pump}}^2 + d_{\text{Stokes}}^2)}{\pi w_x w_y c \epsilon_0 \hbar^2}} \quad (25)$$

$$\Rightarrow \Omega_{\text{eff}}\delta t = \sqrt{\frac{2(d_{\text{Pump}}^2 + d_{\text{Stokes}}^2)}{\pi w_y c \epsilon_0 \hbar^2 v_{\parallel}^2}} \sqrt{P w_x} \equiv A \sqrt{P w_x} \quad (26)$$

$$\Rightarrow P w_x = A^{-2} \quad (27)$$

where we have assumed $\delta t = w_x/v_{\parallel}$ with v_{\parallel} the molecule forward velocity. If we assume a laser beam waist of 2 cm in the long direction as before and a molecule forward velocity of 200 m/s, we can calculate A for those states where we know both transition dipole matrix elements. This isn't many of the levels, but for C we find $A \approx 3 \times 10^4$. If we assume that we have a waist of 10 μm we require 0.1 mW of power in each beam such that $\Omega_{\text{eff}}\delta t = 1$. If we want, for example, $\Omega_{\text{eff}}\delta t = 10$, where we can reasonably expect the criterion to be satisfied, we will then require $P \approx 10$ mW. This is approximately in line with observations from $X \rightarrow C \rightarrow H$ STIRAP — the transfer efficiency saturates at around 10 mW of $X \rightarrow C$ power.

A second requirement for efficient STIRAP, particularly relevant to our application, is that the two-photon linewidth of the transition, $\sigma_{2\gamma}$, is large compared to the two-photon Doppler linewidth, $\sigma_{2\gamma\text{Dopp}}$. If we take the velocity distribution of the beam before the lens (where it is larger) we can then generate the two-photon Doppler linewidth for a given pair of transitions. Let's assume we use the C state as an intermediate. The two-photon detuning for a component of transverse velocity along the laser beams, v , is given by

$$\delta = v(\lambda_{\text{Pump}}^{-1} - \lambda_{\text{Stokes}}^{-1}) \approx 0.6v \text{ MHz}. \quad (28)$$

We can then rescale the distribution given in the top plots of Fig. 17 to give the following graph: We must now demand that we can perform efficient STIRAP over this range of two-photon detunings, i.e. we must estimate the width of the two-photon lineshape. In general this is a non-trivial task, as the lineshape depends on specifics of the system such as the powers in each beam or the one-photon detuning. (For example, it is known, and we found in doing $X \rightarrow C \rightarrow H$ STIRAP, that the lineshape can be strongly affected by asymmetric Rabi frequencies caused by asymmetric transition dipole moments — see e.g. [5, 6] for more details.) In Ref. [7] (following Eq. 21) a simple expression for the two-photon half-width is given:

$$\sigma_{2\gamma}/2 = \frac{2V_m}{\sqrt{\gamma\delta t}} \quad \gamma\delta t \gg 1, \quad (29)$$

where V_m is 'a characteristic value' of the pump and Stokes Rabi frequencies (for conservatism let's assume it to be the smaller of the two), γ is the decay rate of the intermediate state (for now I shall take this as the intermediate state decay rate, although strictly they define it as decay rate out of the 3-level system) and δt is the transit time in the STIRAP beams. Unfortunately, this expression is only valid for $\gamma\delta t \gg 1$, which when using C as the intermediate state, is not valid ($\gamma\delta t \approx 2 \text{ MHz} \times 50 \text{ ns} = 0.1$). They state that 'in the opposite case' the halfwidth is given by

$$\sigma_{2\gamma}/2 \approx 1.3V_m. \quad (30)$$

A similar expression is also derived in Ref. [5] Eq. 36a, although they state it as a full width. Let's err on the side of conservatism and assume this to be our FWHM. Using this expression the two-photon linewidth is then simply

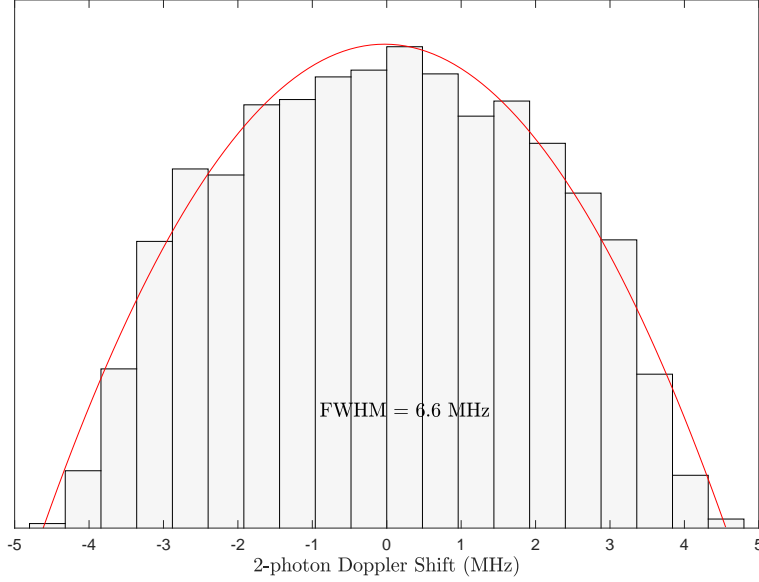


Figure 19: Simulated two-photon Doppler lineshape for STIRAP from X to Q via C for molecules 5 cm upstream of the magnetic lens.

prescribed by the Rabi frequencies applied. If as before we assume equal powers in each beam the two-photon width of the STIRAP transfer is equal to the two-photon Doppler width for a laser power of

$$P_3 = \frac{\sigma_{2\gamma}^2 \pi w_x w_y \epsilon_0 c \hbar^2}{2 \min(d_{\text{pump}}, d_{\text{Stokes}})^2}. \quad (31)$$

Again, these are calculated, and I include their values in Table 1. Here, the values seem rather small, although one should note that it would likely be necessary to ensure that the 2-photon linewidth is significantly larger than the 2-photon Doppler width — it is likely that the transfer efficiency would be significantly reduced towards the edges of the 2-photon lineshape. Then, the power should increase by a factor $\sigma_{2\gamma}^2 / \sigma_{2\gamma\text{Dopp}}^2$. We have also ignored the reduction in intensity of the STIRAP laser beams which occurs in the direction orthogonal to the molecule beam. The power should then inversely with the reduction in intensity. Perhaps this criterion is better evaluated via more sophisticated methods.

6 Adiabaticity

At first blush it would seem that adiabaticity should be no problem for us: — the field gradients are moderate and in particular we don't anticipate any large gradients in regions of small Zeeman splitting. However, when one considers the Omega-doublet structure of our molecule it might present a problem. Fig. 20 shows the energy levels of the $|Q, J = 2\rangle$ state. We note that there is a very small splitting between the opposite parity Omega-doublets and any mixing between these states would jeopardise the subsequent state preparation, which would in general only address molecules in one doublet. In particular, an electric field transverse to the quantisation axis (i.e. transverse to the magnetic field) could cause such mixing. In order to prevent this, we consider applying an electric field along the quantisation which is stronger than any residual transverse fields. This electric field configuration (another hexapole) can be achieved quite easily if we apply voltages to the magnet segments, as shown in Fig. 21.

After calculating this field configuration we should examine whether or not the molecules do indeed experience an electric field along their quantisation axis during their passage through the lens. To do this I adapted my simulation to a 'fully 3D' version — the E- and B-field are computed in COMSOL, and then during trajectory simulation I interpolate based on this data. I also add in computation of the trajectories in the fringing fields 5 cm

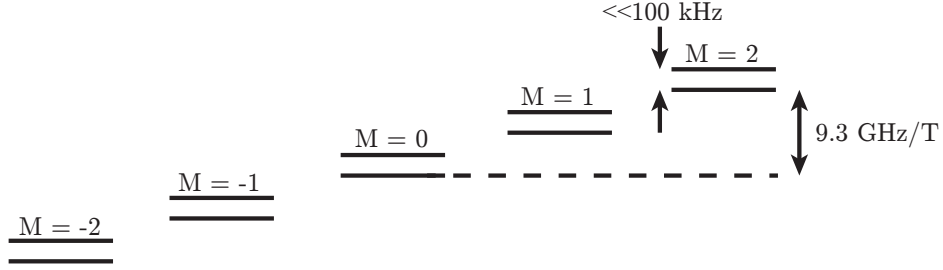


Figure 20: Energy level structure of the $|Q, J = 2\rangle$ state.

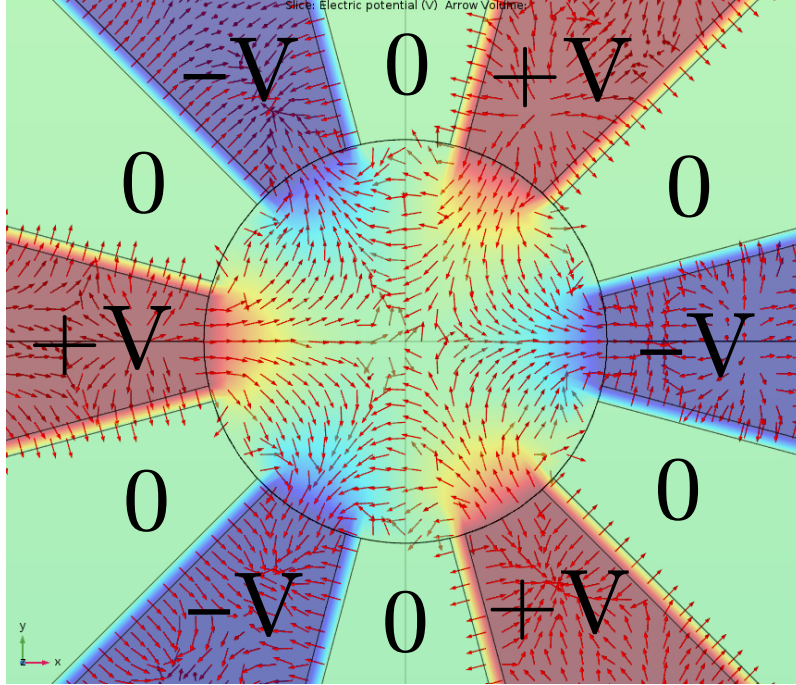


Figure 21: Electric field hexapole configuration produced by applying voltages to magnet segments.

before and after the lens. As a figure of merit I compute the components of E-field parallel and perpendicular to the quantisation axis, i.e.

$$E_{\parallel} = \vec{E} \cdot \hat{B}, \quad (32)$$

$$E_{\perp} = |\vec{E} \times \hat{B}|. \quad (33)$$

(Where $\sqrt{E_{\parallel}^2 + E_{\perp}^2} = |\vec{E}|$.) Performing this analysis we find that

7 Construction

I have created some preliminary designs of a structure to create a hexapole Halbach array, which is shown in Fig. 22. 12 arcs of neodymium magnet are arranged in a circular pattern to produce the hexapole Halbach array. The arcs are pushed into an aluminium frame where they are separated by 1 mm. Ideally this frame is produced such that the segments fit snugly inside, either via a wire EDM or potentially waterjet. The aluminium frame has four circular pockets, one at each corner. On the underside of the frame there are corresponding circular extrusions (these would of course be milled, not extruded). At these four corners there are also thru holes. Multiple layers are stacked on top of each other, mating via the extrusions/pockets at the four corners. Once stacked together, aluminium plates

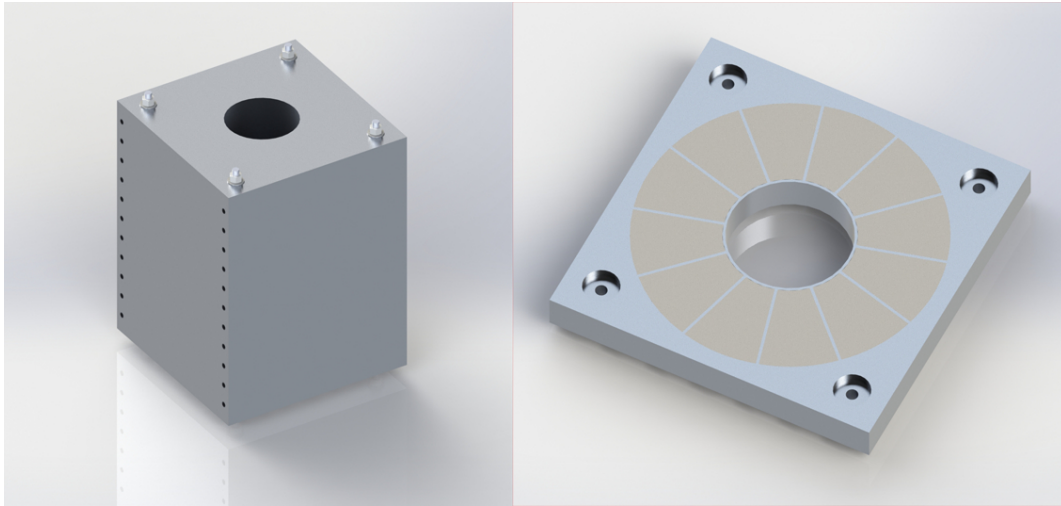


Figure 22: Left: Single layer of cylindrical array. 12 arcs of neodymium magnet are pressed into an aluminium frame. Right: Overall assembly for a cylindrical Halbach array. A series of the layers shown in the left-hand image are stacked together.

are placed on either end, threaded rods are passed through the holes at each corner, and the whole assembly is then clamped together.

This particular design is based on the stock items available here. Each segment costs around \$30 when buying a large number, which makes each layer (1 in. thick) cost \$360.

Before construction it would be important to think a little about how best to actually put the array together, particularly if a great deal of force is required. Emine and Sid would surely have some advice in this regard. In particular one should decide whether or not to glue the segments into place — it seems that this would be preferable. After constructing the individual layers, they can be stacked and unstacked in a modular manner. Again significant force would probably be required to assemble the layers.

References

- [1] J. Mol. Spectr. **113**, 93–104 (1985)
- [2] Phys. Rev. A **90**, 062503 (2014)
- [3] J. Quant. Spectrosc. Radiat. Transfer **12**, 1569–1590 (1972)
- [4] J. Chem. Phys. **119**, 798–805 (2003)
- [5] Phys. Rev. A **81**, 053415 (2010)
- [6] Phys. Rev. A **93**, 052110 (2016)
- [7] Opt. Comm. **140**, 231–236 (1997)